8
The G-band and the Time-Dependent Perturbations

In Chapter 7 we learned how to treat strain effects in the G-band of graphene-related systems. This includes pressure effects and other mechanical deformations, such as bending the graphene sheet to "build" a carbon nanotube. The next step would be the study of temperature (T) and doping-dependent effects. However, for an accurate description of such effects in graphene related systems, it is important to understand the dynamics of electron–phonon coupling because the so-called Born–Oppenheimer (or adiabatic) approximation is not valid for graphene.

In this chapter we review the detailed G-band properties connected to dynamic effects of the electron–phonon coupling by introducing the concepts of the Kohn anomaly and by discussing the effect of temperature and doping on the electron–phonon coupling. These effects have to be derived within time-dependent perturbation theory, as explained in Section 8.1, where we discuss the breakdown of the adiabatic approximation. In Section 8.2 we introduce the effect of changing temperature and show how time-dependent perturbation theory applies for interpreting experimental studies of doping by using a gate, as well as by studying temperature-related effects. We address graphene in Section 8.3 and SWNTs in Section 8.4.

8.1
Adiabatic and Nonadiabatic Approximations

To put the time-dependent perturbations in the context of the general vibrational properties, we stress that in most cases, atomic vibrations are treated in the so-called adiabatic approximation. We can use the adiabatic approximation when the electrons move sufficiently fast so that they can follow the small motion of the heavy nuclei. Then the motion of the electrons can be expressed as a function of the *position* of the atom (not as a function of the *momentum* of the atom). However, when the atomic motion is much faster than the time for electron-momentum relaxation by the electron–phonon interaction, the adiabatic approximation is no longer valid. This problem is pictured in Figure 8.1 where the differences in electronic behavior in the adiabatic vs. nonadiabatic approaches are highlighted, respectively, in Figure 8.1b,c [248].

Raman Spectroscopy in Graphene Related Systems. Ado Jorio, Riichiro Saito, Gene Dresselhaus, and Mildred S. Dresselhaus

ISBN: 978-3-527-40811-5

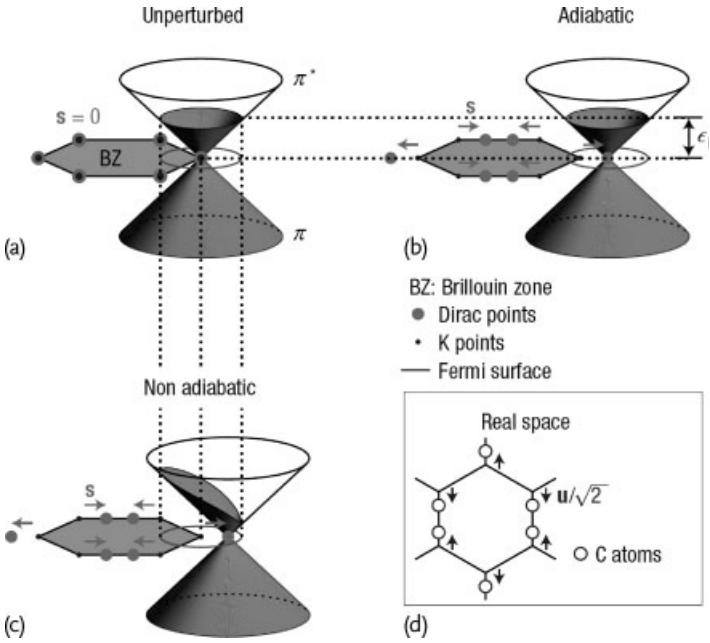

Figure 8.1 Schematic π-band structure of graphene near the high-symmetry *K* point of the Brillouin zone. Here the graphene is doped and the filled electronic states are shown in gray. (a) Bands of the perfect crystal. The Dirac point is at the K point, the electronic states are filled up to the Fermi energy ϵ_{F}, and the Fermi surface is a circle centered at *K*. (b) Bands in the presence of a Γ_6^+ (E_{2g}) lattice distortion. The Dirac points are displaced from *K* by $\pm s$. Within the adiabatic approximation, the electrons remain in the instantaneous ground state: the bands are filled up to the Fermi energy ϵ_F and the Fermi surface follows the Dirac point displacement. The total electron energy does not depend on *s*. (c) Bands in the presence of a Γ_6^+ (E_{2g}) lattice distortion. In the nonadiabatic case, the electrons do not have time to relax their momenta to follow the instantaneous ground state. In the absence of scattering, the electron momentum is conserved and a state with momentum *k* is occupied if the state with the same *k* was occupied in the unperturbed case. As a consequence, the Fermi surface is the same as in the unperturbed case and does not follow the Dirac cone displacement. The total electron energy increases with s^2, resulting in the observation of a Γ_6^+-phonon softening. (d) Atomic displacement pattern of the Γ_6^+ (E_{2g}) phonon. The atoms are displaced from their equilibrium positions by $\pm u/\sqrt{2}$. Note that the displacement pattern of the Dirac points (in reciprocal space) is identical to the displacement pattern of the carbon atoms (in real space) [248].

The G-band frequency of $\omega_{\mathrm{G}} \sim 1584\,\mathrm{cm}^{-1}$ corresponds to 22 fs as the period for atomic motions. In fact, coherent phonon spectroscopy measurements [43] which can observe oscillations in the transmission probability of light in a material as a function of time at the frequency of G-band phonons, observed a 47 THz oscillation for the G-band which indeed corresponds to 22 fs. The measured electron-momentum relaxation times, due to impurity, electron–electron and electron–phonon scattering processes are all on the order of a few hundred femtoseconds, as deduced

from the electron mobility in graphene [249] and from ultrafast spectroscopy measurements in graphite [250, 251]. Thus the virtually excited electrons do not have sufficient time to relax their momenta to reach the instantaneous adiabatic ground state (see the schematics for a nonadiabatic process in Figure 8.1) [248]. Electrons and phonons are thus strongly coupled, and cannot be treated within the usual adiabatic approximation, thus generating a strong G-band frequency dependence on structure, doping (changes in the Fermi level) and temperature.

8.2
Use of Perturbation Theory for the Phonon Frequency Shift

This section starts in Section 8.2.1 by describing the general effect of temperature (T) of phonons, and by highlighting the importance of T on the Fermi distribution. In Section 8.2.2 perturbation theory is used to calculate the phonon frequency shift due to the electron–phonon interaction under nonadiabatic conditions, showing the effect of changes in the Fermi distribution as a function of gate voltage and temperature.

8.2.1
The Effect of Temperature

The change in the phonon frequencies with temperature is a general manifestation of anharmonic terms in the lattice potential energy, which are responsible for the phonon–phonon coupling of the phonon population and of the thermal expansion of the crystal [252]. The effect of temperature on the G-band frequency for different sp^2 nanocarbons has been measured and is represented by:

$$\omega_{\mathrm{G}} = \omega_{\mathrm{G}}^{0} + \chi T \,, \tag{8.1}$$

where ω_{G}^{0} is the G-band frequency in the limit $T \rightarrow 0$ and χ is the coefficient for the temperature-dependent correction to ω_{G} (to first order). Table 8.1 gives the values of χ for different sp^2 nanocarbons, found in the literature. Calizo *et al.* [253] found $\omega_{\mathrm{G}}^{0} = 1584\,\mathrm{cm}^{-1}$ and $1582\,\mathrm{cm}^{-1}$ for 1-LG and 2-LG, respectively. They describe the temperature-dependent effects as roughly divided into the *self-energy* shift due to the anharmonic coupling of the phonon modes and to the shift due to the thermal expansion of the crystal,[1)] that is [253]:

$$\omega_{\mathrm{G}} - \omega_{\mathrm{G}}^{0} = (\chi_T + \chi_V)\Delta T = \left(\frac{\partial \omega}{\partial T}\right)_V \Delta T + \left(\frac{\partial \omega}{\partial V}\right)_T \Delta T \,. \tag{8.2}$$

In fact, for highly oriented pyrolytic graphite (HOPG) it has been considered that the thermal expansion occurs mainly along the c axis, and the in-plane thermal

1) The thermal expansion of a crystal is also a result of anharmonicity. However, the thermal expansion is also related to changes of the elastic force constants with volume, and these two different physical mechanisms can be considered separately.

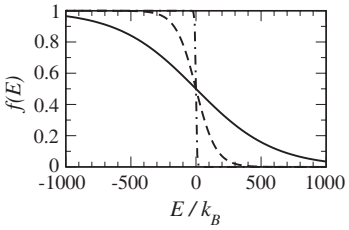

Figure 8.2 The Fermi–Dirac distribution at 300 K (solid), 77 K (dashed), and 4 K (dot-dashed) as a function of energy scaled by k_B, the Boltzmann constant.

Table 8.1 The temperature coefficient in Eq. (8.1) for different sp^2 carbons.

Sample	χ (cm^{-1}/K)	Reference
1-LG	−0.0162	[253]
2-LG	−0.0154	[253]
SWNT	−0.0189	[254]
DWNT	−0.022	[255]
HOPG	−0.011	[256]

expansion is negligible, that is, $\chi = (\chi_T + \chi_V) \approx \chi_T$ for HOPG [256]. The ω_G shifts with temperature have been used to obtain the thermal conductivity of graphene, as explained in [257].

However, for an accurate description of the G-band frequency behavior, we have to consider the electron–phonon coupling, and that the electron population in crystalline structures depends on temperature. This dependence is described by the Fermi–Dirac distribution $f(E)$, which gives the probability that an orbital at energy E will be occupied in an ideal electron gas in thermal equilibrium [95]:

$$f(E) = \frac{1}{\exp[(E-\mu)/k_B T] + 1}\,, \tag{8.3}$$

where T is the temperature in degrees Kelvin (K), k_B is the Boltzmann constant, and the quantity μ is the chemical potential. At absolute zero temperature, the chemical potential is equal to the Fermi energy ($\mu = E_F$). In general, $f(E) = 1/2$ at $E = \mu$ for Eq. (8.3) and Figure 8.2 shows $f(E)$ for three temperatures of interest. At $T = 0$, the occupation probability is $f(E) = 1$ up to the Fermi level, above which the occupation probability drops rapidly. When the temperature increases, there is a spread in the occupation probability around E_F (see Figure 8.2). These changes in carrier occupation will affect the G-band frequency, as discussed in the following sections.

8.2.2
The Phonon Frequency Renormalization

Within the framework of time-dependent perturbation theory, we consider that when the phonon can excite an electron–hole pair (see Figure 8.3) by the electron–phonon interaction, this virtual process[2] gives rise to a phonon energy renormalization that depends on the electronic structure, the Fermi level and the temperature [141, 196, 258, 259]. The phonons then renormalize the electron energies,[3] while the electrons renormalize the phonon energies.[4] Both of these perturbations occur over a longer time than that observed in Raman spectra, which is on the order of 1 s, and thus we can observe these phenomena in Raman spectra. This electron–phonon coupling gives rise to a controllable modification to the G-band frequency as a function of the gate voltage, and this modification depends strongly on the geometrical structure of the nanomaterial, which applies to both carbon nanotubes and graphene.

The phonon frequency shift due to the electron–phonon (el–ph) interaction of the Γ-point LO- and iTO-phonon modes for graphene (and also for SWNTs) can be calculated by second-order perturbation theory. The phonon energy including the el–ph interaction can be written as:

$$\hbar\omega_\lambda = \hbar\omega_\lambda^{(0)} + \hbar\omega_\lambda^{(2)} , \tag{8.4}$$

(λ = LO, iTO) where $\omega_\lambda^{(0)}$ is the unperturbed phonon frequency without consider-

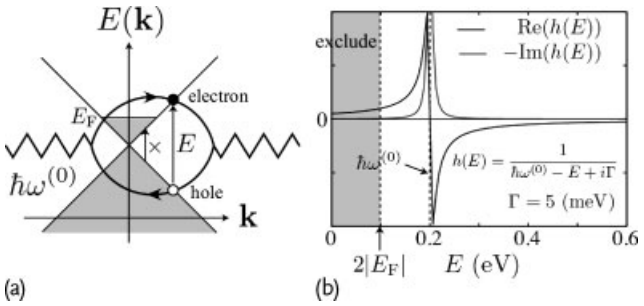

Figure 8.3 (a) An intermediate electron–hole pair state that contributes to the energy shift of the optical phonon modes is depicted. A phonon mode is denoted by a zigzag line and an electron–hole pair is represented by a loop. The low-energy electron–hole pair satisfying $0 \le E \le 2E_F$ is forbidden at zero temperature by the Pauli principle. (b) The energy-dependent real and imaginary parts of the $h(E)$ correction to the phonon energy by an intermediate electron–hole pair state. Especially the sign of the correction depends on the energy of the intermediate state as given by $h(E)$ (see text in Section 8.2) [260].

2) Here a virtual process means the mixing of the wavefunction of the excited states into the ground state wavefunction in perturbation theory. We here consider the electron–phonon interaction as a perturbation.

3) Through the so-called Peierls-like mechanism, that is, the deformation of the electronic structure due to electron–phonon coupling.

4) Resulting in the so-called Kohn anomaly effect, that is, a deformation of the phonon structure due to electron–phonon coupling.

ation of the el–ph interaction, and $\hbar\omega_\lambda^{(2)}$ is the perturbation term given by second-order perturbation theory

$$\hbar\omega_\lambda^{(2)} = 2\sum_{\boldsymbol{k}} \frac{|\langle \mathrm{eh}(\boldsymbol{k})|\mathcal{H}_{\mathrm{int}}|\omega_\lambda\rangle|^2}{\hbar\omega_\lambda^{(0)} - (E_\mathrm{e}(\boldsymbol{k}) - E_\mathrm{h}(\boldsymbol{k})) + i\Gamma_\lambda} \times [f(E_\mathrm{h}(\boldsymbol{k}) - E_\mathrm{F}) - f(E_\mathrm{e}(\boldsymbol{k}) - E_\mathrm{F})] \quad , \tag{8.5}$$

and is the quantum correction to the phonon energy due to electron–hole pair creation as shown in Figure 8.3a. The factor 2 in Eq. (8.5) comes from the spin degeneracy. In Eq. (8.5), $\langle \mathrm{eh}(\boldsymbol{k})|\mathcal{H}_{\mathrm{int}}|\omega_\lambda\rangle$ is the matrix element for creating an electron–hole pair at momentum $\boldsymbol{k}$ by the el–ph interaction with a $q = 0$ phonon, while $E_\mathrm{e}(\boldsymbol{k})$ ($E_\mathrm{h}(\boldsymbol{k})$) is the electron (hole) energy and Γ_λ is the decay width. In Figure 8.3a, an intermediate electron–hole pair state that has the energy of $E = E_\mathrm{e}(\boldsymbol{k}) - E_\mathrm{h}(\boldsymbol{k})$ is shown. Thus in Eq. (8.5) we need to sum ($\sum_{\boldsymbol{k}}$) over all possible intermediate electron–hole pair states which can have a much larger energy than the phonon ($E \gg \hbar\omega_\lambda^{(0)}$).

Since $\langle \mathrm{eh}(\boldsymbol{k})|\mathcal{H}_{\mathrm{int}}|\omega_\lambda\rangle$ is a smooth function of $E = E_\mathrm{e}(\boldsymbol{k}) - E_\mathrm{h}(\boldsymbol{k})$ which appears in the denominator of Eq. (8.5), the contribution to $\hbar\omega_{\lambda(2)}$ from an electron–hole pair depends strongly on its energy. In Figure 8.3b, we plot the real part and imaginary part of the denominator of Eq. (8.5), $h(E) = 1/(\hbar\omega^{(0)} - E + i\Gamma)$ as a function of E in the case of $\hbar\omega^{(0)} = 0.2$ eV and $\Gamma = 5$ meV. Here $\mathrm{Re}(h(E))$ has a positive (negative) value when $E < \hbar\omega^{(0)}$ ($E > \hbar\omega^{(0)}$) and the lower (higher) energy electron–hole pair makes a positive (negative) contribution to $\hbar\omega_\lambda^{(2)}$. Moreover, an electron–hole pair satisfying $E < 2|E_\mathrm{F}|$ cannot contribute to the energy shift (shaded region in Figure 8.3a,b) because of the Fermi distribution function $f(E)$ in Eq. (8.5). Thus, the quantum correction to the phonon energy by an intermediate electron–hole pair can be controlled by changing the Fermi energy, E_F (see Figure 8.4b). For example, when $|E_\mathrm{F}| = \hbar\omega^{(0)}/2$, then $\hbar\omega_\lambda^{(2)}$ takes a minimum value at zero temperature since all positive contributions to $\hbar\omega_\lambda^{(2)}$ are suppressed in Eq. (8.5) (e. g., see dashed line in Figure 8.4b). Since $\mathrm{Re}(h(E)) \approx -1/E$ for $E \gg \hbar\omega^{(0)}$, all high energy intermediate states contribute to phonon softening if we include all the electronic states in the system. Here we introduce a cut-off energy at $E_\mathrm{c} = 0.5$ eV as $\sum_{\boldsymbol{k}}^{E_\mathrm{e}(\boldsymbol{k})<E_\mathrm{c}}$ in order to avoid such a large energy shift in Eq. (8.5). The energy shift due to the high-energy intermediate states ($\sum_{\boldsymbol{k}}^{E_\mathrm{e}(\boldsymbol{k})>E_\mathrm{c}}$) can be neglected by renormalizing $\hbar\omega^{(0)}$ so as to reproduce the experimental results of the observed Raman spectra [38, 261] since the contribution from $E_\mathrm{e}(\boldsymbol{k}) > E_\mathrm{c}$ just gives a constant energy shift to $\hbar\omega^{(2)}$. These results do not depend on the selection of the cut-off energy,[5] since E_c is much larger than $\hbar\omega^{(0)}$.

The $\mathrm{Im}(h(E))$ in Figure 8.3b is nonzero only very close to $E = \hbar\omega^{(0)}$, which shows that the phonon can resonantly decay into an electron–hole pair with the

5) A cut-off energy is generally taken for setting the upper-limit of the integration in calculating a physical property even when the integration has a contribution above the cut-off energy. In order to avoid the cut-off energy dependence of the results, a smooth function is defined for switching off this contribution. Calculating the phonon frequency in a solid essentially contains the electron–phonon interaction in discussions that were given in the 1950s. See details in [38].

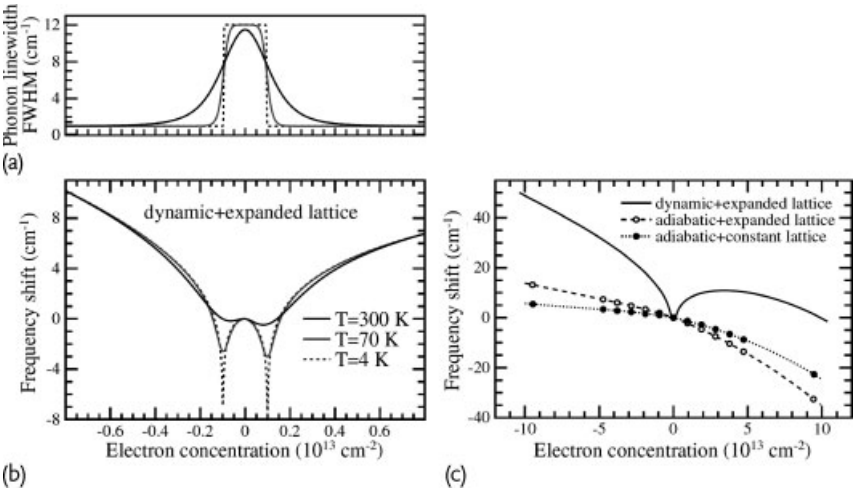

Figure 8.4 (a) Linewidth and (b) frequency of the Raman G-band as a function of the electron concentration. The calculations are made using time-dependent perturbation theory, which considers the dynamic effects (i. e., under the nonadiabatic approximation) and lattice distortion induced by doping. (c) G-band frequency behavior on a larger doping range comparing the expected results for adiabatic vs. nonadiabatic and constant lattice vs. doping induced lattice distortions (extended lattice). Adapted from [258].

same energy as the phonon. It is noted that when $|E_F| > \hbar\omega^{(0)}/2$, then the resonance window width is small, that is $\Gamma_\lambda \approx 0$ at zero temperature, while Γ_λ may take a finite value at a finite temperature (see Figure 8.4a). The plot in Figure 8.3b gives Γ_λ self-consistently[6] calculating $\Gamma_\lambda = -\mathrm{Im}(\hbar\omega_\lambda^{(2)})$ in Eq. (8.5). Figure 8.4a shows the expected behavior of the G-band FWHM by changing the electron concentration (i. e., changing the Fermi level).

The effect of changing temperature on the phonon renormalization is shown in Figure 8.4 by the different line styles, as rationalized by the Fermi distribution related term in Eq. (8.5). As discussed in Section 8.2.1, at $T = 0$ the occupation probability is $f(E) = 1$ up to the Fermi level, above which the occupation probability drops rapidly. This makes a highly singular dependence for the phonon renormalization and linewidth variation at $E_F = \pm\hbar\omega_G/2$ (see Figure 8.4a,b). When the temperature increases, there is a spread in the occupation probability around E_F (see Figure 8.2), thus smoothing out the singularities at $E_F = \pm\hbar\omega_G/2$.[7]

Finally, you may have noticed the asymmetry in the frequency shift in Figure 8.4b for large doping values (e. g., electron concentration $\rightarrow \pm 0.8\times10^{13}$ electrons/cm^{-2}). This asymmetry is clearer in Figure 8.4c where the doping range is extended. The Kohn anomaly effect discussed here occurs within a small doping range, where

6) When the initial value of Γ_λ in Eq. (8.5) is the same as $\mathrm{Im}(\hbar\omega_\lambda^{(2)})$, then we can say that the calculation is self-consistent. The value of Γ_λ depends on the electron–phonon interaction (numerator of Eq. (8.5)). This treatment is equivalent to the treatment of Γ_λ when using the uncertainty relation.

7) The Fermi function $f(E)$ in Eq. (8.5) becomes a smooth function of energy at 300 K (see Figure 8.2).

E_F lies near the K point. When higher doping levels take place, lattice distortion induced by doping dictates the ω_G behavior. From Figure 8.4c we see that lattice distortion induced p doping causes a hardening of ω_G, while n doping causes a softening of ω_G. The difference from *weak* and *strong* doping will be discussed further for gate and chemical doping of SWNTs, respectively (Section 8.4.4). In the case of graphene, up to now only gate doping results are available experimentally, as discussed in the next section.

8.3
Experimental Evidence of the Kohn Anomaly on the G-band of Graphene

In this section the effect of doping on the G-band of single-layer graphene (Section 8.3.1) and on the G-band of double-layer graphene (Section 8.3.2) is explicitly considered.

8.3.1
Effect of Gate Doping on the G-band of Single-Layer Graphene

Experimental observation of the effect of doping on the G-band phonon frequency is shown in Figure 8.5 [196]. The G-band is observed to upshift in frequency (Figure 8.5a,b) and to decrease in linewidth (Figure 8.5c) with doping, as predicted by time-dependent perturbation theory. The physics behind this behavior comes from the Pauli exclusion principle. Under increasing doping, the electron–hole interaction for different energies will be forbidden, thereby decreasing the Kohn anomaly effect. At $T = 0\,\mathrm{K}$, the effect would be abrupt, but for $T \neq 0\,\mathrm{K}$, there is an energy distribution for the carriers and the Kohn anomaly-induced frequency change tends to saturate when the Fermi level is far from $\hbar\omega_\lambda/2$. The two anomalies at $\pm\hbar\omega_G/2$ are not clearly seen in this experiment due to temperature-induced broadening (see Figure 8.4a). However, a gate voltage dependence for the G-band frequency ω_G was measured at $T = 12\,\mathrm{K}$, where phonon anomalies at $E_F = \pm\hbar\omega_G/2$ could be clearly distinguished [262]. The 12 K experiment was, however, carried out on bilayer graphene, where another interesting effect occurs, as described in Section 8.3.2.

8.3.2
Effect of Gate Doping on the G-band of Double-Layer Graphene

In bilayer graphene, the unit cell has 4 C atoms rather than 2, and as a result there are two π and two π^*-bands at the K point (see Figure 2.11). In this case, there will be more than two Kohn anomalies in the G-band gate-dependent frequency renormalization (see schema on the right hand side of Figure 8.6) [262]. When the Fermi energy reaches $\pm\hbar\omega_G/2$, the $\pi - \pi^*$ transition from the valence band to the lower conduction band shown in Figure 8.6(I) is no longer allowed, as it is in single-layer graphene. However, the transition from the now filled lowest energy π^*-band

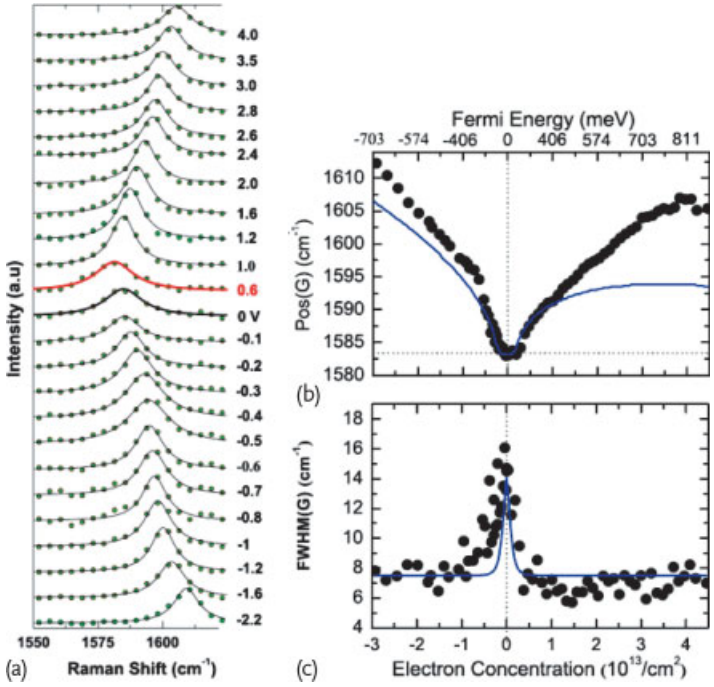

Figure 8.5 The Raman G peak of doped monolayer graphene. (a) The G-band spectra at 295 K for many values of the gate voltage V_g. The red spectrum corresponds to the undoped case, which occurs at $V \neq 0$ due to natural doping of graphene by the environment. (b) The G peak position (frequency) and (c) the linewidth as a function of electron concentration, deduced from the applied gate voltage data. Black circles: measurements; solid line: finite-temperature nonadiabatic calculation. Adapted from [196].

to the higher energy π^*-band, shown by the dashed red arrow in Figure 8.6(II), is possible. When the gate voltage rises further and the Fermi energy reaches the second band, $\pi^* - \pi^*$ transitions are suppressed, as shown in Figure 8.6(III). These effects are seen in the G-band frequency and linewidth of bilayer graphene (see Figure 8.6), where a distinctly different behavior with respect to the monolayer case (see Figure 8.5) is clearly observed for both the G-band frequency and linewidth. Therefore, when discussing graphene systems above, we saw that the renormalization effect changes significantly in going from single-layer to bilayer graphene, and it would change further by increasing the number of layers, although the renormalization effect will become less and less evident with increasing layer number.

8.4
Effect of the Kohn Anomaly on the G-band of M-SWNTs vs. S-SWNTs

The Kohn anomaly is important for systems with an electronic gap smaller than the phonon energy. The Kohn anomaly is, therefore, applicable to the G-band

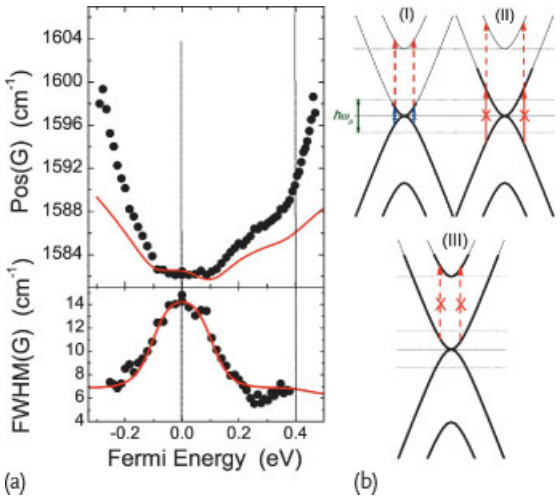

Figure 8.6 (a) Peak frequency (Pos(G)) and linewidth (FWHM(G)) for the Raman G-band feature of doped bilayer graphene vs. Fermi energy. Black circles: measurements; red line: finite-temperature nonadiabatic calculation. (b) Schematics of the electron–phonon coupling at three different doping levels, as indicated by the thicker lines on the electronic bands. Adapted from [262].

in graphene and also in metallic SWNTs. As shown by the "∗" symbols in Figure 7.6, the LO G-band in metallic SWNTs experiences a large renormalization in frequency, due to the what is called a Peierls-like mechanism [124]. This Peierls-like mechanism is, in fact, due to the electron–phonon interaction, as is also the Kohn anomaly effect, but the effect is much stronger in metallic carbon nanotubes than in graphene, due to the phonon confinement that generates a dynamic gap opening. For semiconducting SWNTs, some renormalization occurs related to virtual transitions, but the effect should be minor for S-SWNTs. Furthermore, in SWNTs, because of their spatial confinement effects, there is a rich behavior depending not only on their metal vs. semiconducting behavior, but also on the SWNT diameter and chirality. We discuss these results here.

8.4.1 The Electron–Phonon Matrix Element: Peierls-Like Distortion

In this section we show that the Kohn anomaly is very different for LO and iTO phonons. The effect of the G-band phonons on the electronic structure is evaluated here first for graphene, within the first-neighbor tight-binding model and the adiabatic approximation. The corresponding effect for nanotubes will then be summarized based on quantum confinement and zone-folding effects. Although the extended tight-binding and nonadiabatic approximations are needed for quantitative studies, the simple pedagogic picture described here can account for the fundamentals of the pertinent physical effect.

Consider the matrix elements H_{AA}, H_{AB}, H_{BA}, and H_{BB} evaluated within the framework of the nearest neighbor π-band orthogonal tight-binding model in the linear in u/a approximation (u is the amplitude of phonon displacements, and $a = \sqrt{3}a_{CC} = 0.246$ nm is the graphene lattice constant):

$$H_{AA} = H_{BB} = E_0 + \epsilon \sum_j^3 (u_{Bj} - u_{A0}) \cdot (r_{Bj} - r_{A0})/a_{CC} \,, \tag{8.6}$$

$$H_{AB} = H_{AB}^* = \sum_j^3 [t + \alpha(u_{Bj} - u_{A0}) \cdot (r_{Bj} - r_{A0})/a_{CC}] \times \exp[ik \cdot (r_{Bj} - r_{A0} + u_{Bj} - u_{A0})] \,. \tag{8.7}$$

Here, E_0 is the atomic orbital energy which is set to zero to define our energy scale, $t = -2.56$ eV is the transfer or hopping integral for graphene, $\epsilon = 39.9$ eV/nm is the on-site electron–phonon coupling (EPC) coefficient, $\alpha = 58.2$ eV/nm is the off-site EPC coefficient [222, 263, 264], r_{Aj} and r_{Bj} are the equilibrium atomic positions shown by the gray and green dots in Figure 8.7a, respectively, u_{Aj} and u_{Bj} are the atomic displacements associated with the Γ_6^+ (E_{2g}, G-band) phonon mode represented by arrows in Figure 8.7a, subscript $j = 0, \ldots, 3$ labels the central atom and its three nearest neighbors, $a_{CC} = 0.142$ nm is the interatomic distance and k is the electron wave vector. Upon substituting u_{Aj} and u_{Bj} from the G-band eigenvectors (Figure 8.7a for the LO phonon) into Eq. (8.6) and setting the graphene determinant equal to zero, we find that $k_F(k'_F)$ oscillates at the phonon frequency with a displacement amplitude $\Delta k_F(\Delta k'_F)$ given by:

$$\begin{aligned} \Delta k_F &= -\Delta k'_F = -\frac{2\sqrt{3}\alpha u}{ta}\hat{y} \quad \text{for LO} \,, \\ \Delta k_F &= -\Delta k'_F = +\frac{2\sqrt{3}\alpha u}{ta}\hat{x} \quad \text{for iTO} \,, \end{aligned} \tag{8.8}$$

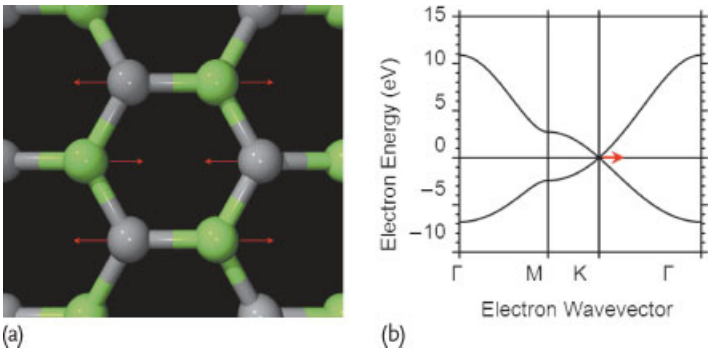

Figure 8.7 (a) Arrows indicate the atomic motions for the G-band mode in graphene. (b) The red arrow indicates the displacement of the $\pi - \pi^*$ crossing point on the $E(\boldsymbol{k})$ diagram when the G-band LO phonon displacement takes place [117].

around the $K(K')$ point in the Brillouin zone [124]. Note that Δk_F and $\Delta k'_F$ are determined by the off-site EPC coefficient α, since the ϵ terms in Eq. (8.6) that are linear in u/a cancel for the u_{Aj} and u_{Bj} vectors [265]. The arrow in Figure 8.7b shows such a Δk_F measurement for the LO phonon. This change in the electronic structure causes a distortion in the electronic matrix element, that is responsible for the EPC.

Now, if we move to metallic nanotubes, the presence of cutting lines in the Brillouin zone due to spatial confinement will play a very important role. For an armchair SWNT in an equilibrium position, a cutting line crosses the K point, and the valence and conduction bands cross (see Figure 8.8a). When a displacement of the G-band iTO phonon takes place (see Figure 8.8b), the $\pi - \pi^*$ crossing point moves along the cutting line direction, and no significant change in the electronic structure occurs. However, when a displacement of the G-band LO phonon takes place (see Figure 8.8c), the $\pi - \pi^*$ crossing point now moves perpendicular to the cutting line direction, thus opening a band gap. This effect changes the total electronic energy of the tube significantly, generating a significant electron–phonon coupling, much stronger than that in graphene. In linear carbon chains, this gap opening decreases the energy enough, so that the phonon softens towards zero frequency and the carbon chain gets distorted (going to the C≡C–C≡C–C bonding configuration from the original C=C=C=C bonding configuration). This distortion is known as the Peierls distortion. In carbon nanotubes, the energy lowering due to the Peierls distortion is not larger than the thermal energy, and therefore

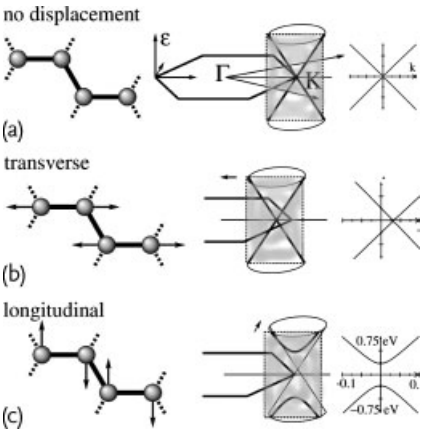

Figure 8.8 (a) Electronic band structure of graphene in the vicinity of the *K* point. Panels (b) and (c) indicate the changes in the electronic band structure caused by the presence of iTO (transverse) and LO (longitudinal) phonon modes. For the A_1(iTO) mode in armchair SWNTs (and the A_1(LO) mode in zigzag SWNTs), the crossing point shifts away from K towards the Γ point. For the A_1(LO) mode in armchair nanotubes (and the A_1(iTO) mode in zigzag tubes), the crossing point moves perpendicular to the line ΓK, opening a band gap. The thick lines indicate the band structure of an armchair tube obtained by intersecting the gray plane with the two cones. Adapted from [124].

the tube does not distort.[8] However, the LO phonon mode in the nanotube suffers a strong renormalization effect, exhibiting a significant softening in the phonon frequency. The same holds for zigzag and chiral metallic nanotubes but to a lesser degree. Although the cutting line for this case will have a different direction, the Δk_F will change as well, so that the overall picture remains similar. It is similar but not exactly the same, because a small correction will have to be considered when going beyond the first-neighbor tight-binding model, since curvature effects generate a mini-gap opening in non-armchair SWNTs, which can be explained by the extended tight-binding electron–phonon coupling model [117, 222].

8.4.2
Effect of Gate Doping on the G-band of SWNTs: Theory

In Figure 8.9, we show calculated results for $\hbar\omega_\lambda$ LO and TO phonons as a function of E_F for a (10, 10) armchair nanotube generated by gate doping. Here we take values of 1595 cm^{-1} and 1610 cm^{-1} for $\hbar\omega_\lambda^{(0)}$, for the λ = iTO and λ = LO modes, respectively. The energy bars in Figure 8.9 denote Γ_λ values for the decay width, and the extended tight-binding scheme is used to calculate $E_e(\boldsymbol{k})$, $E_h(\boldsymbol{k})$, and the electron wavefunction for $\langle \mathrm{eh}(\boldsymbol{k})|\mathcal{H}_{\mathrm{int}}|\omega_\lambda\rangle$ [267]. Here the el–ph matrix element [203] was obtained using the deformation potential, derived on the basis of density-functional theory by Porezag *et al.* [264]. To obtain the phonon eigenvector, the force constant parameters calculated by Dubay and Kresse [116] were used for the dynamical matrix. The resulting $\hbar\omega_\lambda$ is shown as a function of E_F at room temperature (T = 300 K) and at T = 10 K in Figure 8.9a,b, respectively, where $E_F \neq 0$ is related to gate doping with respect to the equilibrium position at $E_F = 0$, occurring when E_F is at the band crossing point (K point in graphene). It is seen that the iTO mode does not exhibit any energy change, while the LO mode shows both an energy shift and broadening. As we have mentioned above, the minimum energy occurs at $|E_F| = \hbar\omega^{(0)}/2$ ($\approx$ 0.1 eV). There is also a local maximum for the spectral peak at $|E_F| = 0$. The broadening for the LO mode occurs within $|E_F| \leq \hbar\omega^{(0)}/2$ for the lower temperature (10 K), while the broadening has a tail at room temperature for $|E_F| \geq \hbar\omega^{(0)}/2$ in Figure 8.9 [260]. For large $|E_F|$ values, the Kohn anomaly effect is gone and $\omega_G^{LO} > \omega_G^{iTO}$, as expected in the time-independent picture (Section 7.3.3) and is the behavior that is generally observed for semiconducting SWNTs.

A continuum model for electrons in a carbon nanotube has been used [260] to explain the lack of an energy shift of the iTO modes for armchair nanotubes. In this work it is shown that the electron–phonon (el–ph) matrix element for electron–hole pair creation by the (A_1) LO and iTO phonon modes is given by:

$$\begin{aligned} \langle \mathrm{eh}(\boldsymbol{k})|\mathcal{H}_{\mathrm{int}}|\omega_{\mathrm{LO}}\rangle &= -igu\sin\theta(\boldsymbol{k}) , \\ \langle \mathrm{eh}(\boldsymbol{k})|\mathcal{H}_{\mathrm{int}}|\omega_{\mathrm{iTO}}\rangle &= -igu\cos\theta(\boldsymbol{k}) , \end{aligned} \tag{8.9}$$

8) In the case of polyene encapsulated in a SWNT, however, the Peierls distortion is significant [266].

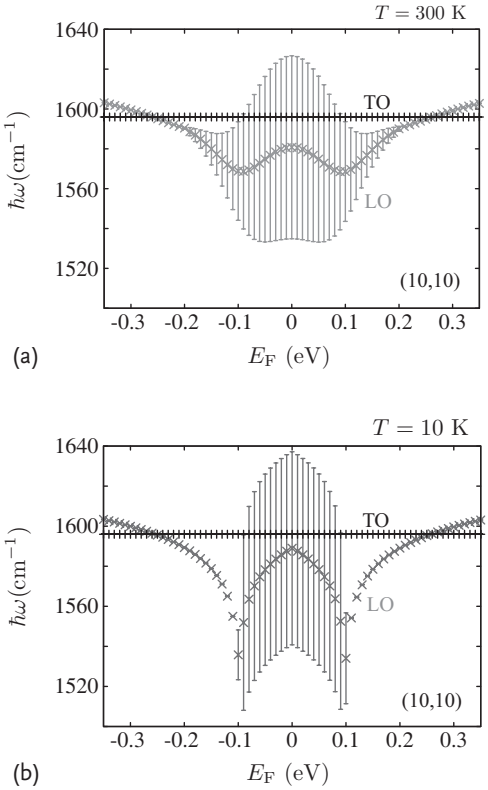

Figure 8.9 The E_F dependence of the LO (gray curve) and iTO (black curve) phonon energy in the case of the (10, 10) armchair nanotube. Part (a) is calculated at room temperature and (b) is at 10 K. Only the energy of the LO mode is shifted, with the iTO mode frequency being independent of E_F. The decay width (Γ_λ) in Eq. (8.5) is plotted as an error-bar [260].

where u is the phonon amplitude, and g is the el–ph coupling constant. Here $\theta(\boldsymbol{k})$ is the angle for the polar coordinate around the K (or K') point in the 2D Brillouin zone, in which the $\boldsymbol{k} = (k_1, k_2)$ point is taken to be on a cutting line for a metallic energy sub-band. The k_1 (k_2) axis is taken in the direction of the nanotube circumferential (axis) direction (see Figure 8.10). Equation (8.9) shows that the matrix element $\langle \mathrm{eh}(\boldsymbol{k})|\mathcal{H}_{\mathrm{int}}|\omega_\lambda\rangle$ depends only on $\theta(\boldsymbol{k})$ but not on $|\boldsymbol{k}|$, which implies that the dependence of this matrix element on E is negligible. For an armchair nanotube, even when considering the curvature-induced distortions, the cutting line for its metallic energy band still lies on the k_2 axis [268]. Thus, we have $\theta(\boldsymbol{k}) = \pi/2$ $(-\pi/2)$ for the metallic energy sub-band, which has $k_1 = 0$ and $k_2 > 0$ ($k_2 < 0$). Then, Eq. (8.9) tells us that only the LO mode couples to an electron–hole pair and the iTO mode is not coupled to an electron–hole pair for armchair SWNTs.

In Figure 8.11a, we show calculated results for $\hbar\omega_\lambda$ as a function of E_F for a (15, 0) metallic zigzag nanotube [260]. In the case of zigzag nanotubes, not only the LO mode but also the iTO mode couples to electron–hole pairs. The spectral peak

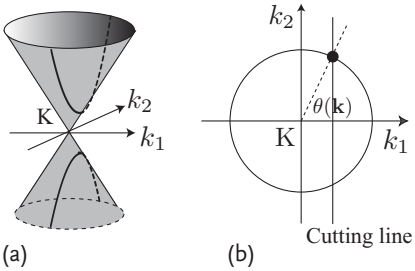

Figure 8.10 (a) Cutting line near the *K* point for an armchair nanotube. The k_1 (k_2) axis is selected as the nanotube circumferential (in-plane) direction. The amplitude for electron–hole pair creation depends strongly on the relative position of the cutting line from the *K* point. (b) If the cutting line crosses the *K* point, then the angle $\theta(\boldsymbol{k})$ ($\equiv \arctan(k_2/k_1)$) takes $\pi/2$ ($-\pi/2$) values for $k_2 > 0$ ($k_2 < 0$). In this case, the LO mode strongly couples to an electron–hole pair, while the iTO mode is decoupled from the electron–hole pair according to Eq. (8.9) [260].

position for the iTO mode is upshifted for $E_F = 0$, since $\mathrm{Re}(\hbar\omega(E))$ for $E < \hbar\omega_{iTO}$ contributes to a positive frequency shift. It has been shown theoretically [268] and experimentally [269] that, even for "metallic" zigzag nanotubes, a finite curvature opens a small energy gap. When the curvature effect is taken into account, the cutting line does not lie on the *K* point, but it is then shifted from the k_2 axis. In this case, $\cos\theta(\boldsymbol{k}) = k_1/(k_1^2 + k_2^2)^{1/2}$ is nonzero for the lower energy intermediate electron–hole pair states since $k_1 \neq 0$. Thus, the iTO mode can couple to the low energy electron–hole pair which makes a positive energy contribution to the phonon energy shift. The high energy electron–hole pair is still decoupled from the iTO mode since $\cos\theta(\boldsymbol{k}) \to 0$ for $|k_2| \gg |k_1|$. Therefore, when $|E_F| \leq \hbar\omega_{iTO}^{(0)}/2$, then $\hbar\omega_{iTO}$ increases by a larger amount than does $\hbar\omega_{LO}$. The iTO mode for the small diameter zigzag nanotubes couples strongly to an electron–hole pair because of the stronger curvature effect for small diameter SWNTs. In Figure 8.11b, we show the diameter (d_t) dependence of the $\hbar\omega_\lambda$ for zigzag nanotubes for $E_F = 0$ not only for metallic SWNTs, but also for semiconducting SWNTs. In the case of the S-SWNTs, the LO (iTO) mode appears around 1600 (1560) cm^{-1} without any broadening. Only metallic zigzag nanotubes show an energy shift, and the energy of the LO (iTO) mode decreases (increases) as compared to the semiconducting tubes. In Figure 8.11c, we show a curvature-induced energy gap E_{gap} as a function of d_t for metallic zigzag tubes. The results show that higher (lower) energy electron–hole pairs contribute effectively to the LO (iTO) mode softening (hardening) in metallic nanotubes. In the case of semiconducting nanotubes, we may expect that there is a softening for the LO and iTO modes according to Eq. (8.9). However, the softening is small as compared with that of the metallic nanotubes because the energy of the intermediate electron–hole pair states is much larger than $\hbar\omega_\lambda^{(0)}$ in this case.

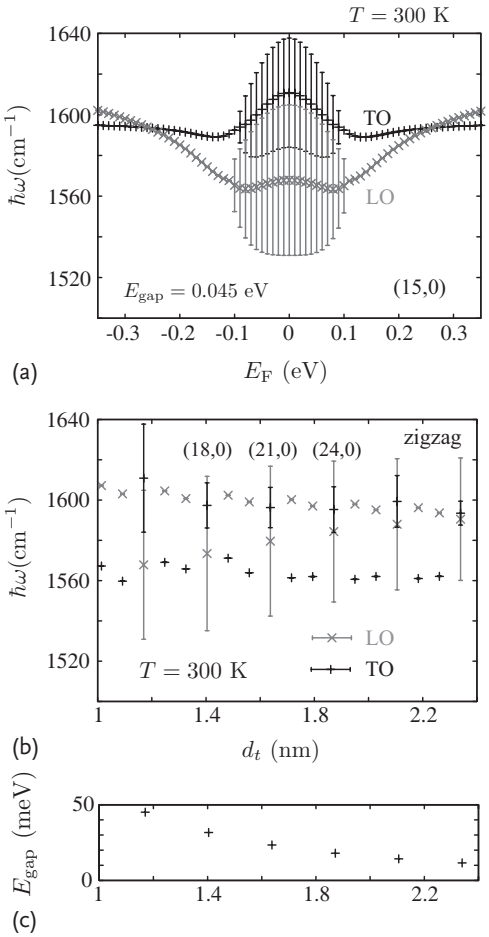

Figure 8.11 (a) The calculated E_F dependence of the LO (gray symbols) and iTO (black symbols) phonon frequency for a (15, 0) zigzag nanotube. The frequency of not only the LO mode, but also that of the iTO mode, is shifted due to the curvature effect. The error bars indicate the phonon linewidth. (b) Diameter d_t dependence of the G-band optical phonon frequencies for zigzag nanotubes, including zigzag semiconducting and metallic nanotubes as well as LO and TO modes. (c) The diameter dependence of E_{gap}, where E_{gap} denotes the curvature-induced mini-energy gap [260].

8.4.3 Comparison with Experiments

Before the Kohn anomaly was discussed in the context of graphene and carbon nanotubes, several experimental works had already reported the Fermi level dependence of the LO and iTO modes of bundles and ensembles of carbon nanotubes [48, 49, 270]. These experiments showed a significant change in frequency and linewidth of the broad feature in the G-band associated with metallic nan-

otubes as E_F was varied. Experiments varying the Fermi level of individual metallic carbon nanotubes [261, 271, 272] later provided more insight into the behavior of the individual modes. In Figure 8.12 we show an experimental intensity map of the G-band spectrum of an individual metallic nanotube as a function of an electrochemical gate voltage. Here there are two distinguishable peaks, a higher frequency mode that does not change appreciably either in frequency or in linewidth as a function of gate voltage, and a broad lower frequency peak, assigned to the LO mode, that upshifts and narrows in linewidth as positive or negative charges are induced on the nanotube.

Unlike the case of graphene, a Kohn anomaly is predicted in metallic carbon nanotubes even in the adiabatic limit. However, use of the adiabatic approximation misses out on key features in the energy range close to the phonon energy. The two signatures of nonadiabatic effects in the Kohn anomaly are: (1) an energy window $E_F < |\hbar\omega_{LO}|$ within which the LO phonon peak is broadened due to the creation of real electron–hole pairs, and (2) a characteristic "W" lineshape of the LO frequency vs. E_F curve caused by the two singularities located at $E_F = \pm\hbar\omega_{LO}$ rather than a single singularity at $E_F = 0$, as predicted within the adiabatic approximation. The data in Figure 8.12 exhibits the characteristic broadening window for metallic SWNTs; however, the "W" shape from the two singularities is not resolved, most likely because of inhomogeneous charging due to trapped charges on the substrate which will result in a smearing of E_F. A more recent experiment [273] using pristine suspended nanotubes that were gated electrostatically was able to resolve this feature in the frequency of the LO mode.

The experiment in Figure 8.12 captures the behavior of the strongly coupled LO mode. The weakly coupled TO mode, if identified at all, is reported to exhibit a flat frequency vs. gate voltage behavior around the Dirac point. This peak has not received much attention, since the TO mode intensity is weak, rendering it difficult

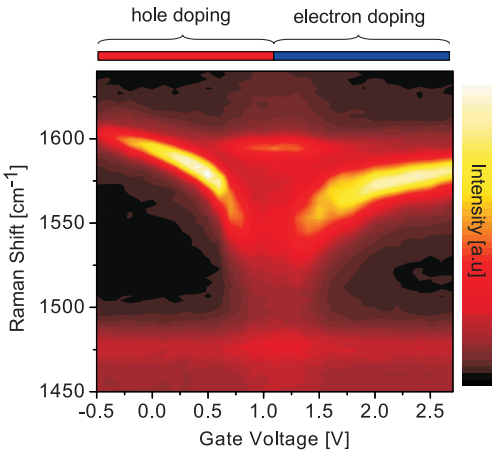

Figure 8.12 Experimental intensity plot of the G-band spectrum of a metallic SWNT as a function of electrochemical gate voltage. The charge neutrality point corresponding to the Dirac point is 1.2 V [261].

to monitor, especially when the G^+ and G^- features lie close to each other in energy. The intensities of the LO and TO modes are known to depend on the chiral angle, with the TO mode being completely silent in the limit of $\theta \rightarrow 0°$ for a zigzag nanotube [272, 274]. Nonetheless, as shown in Figures 8.9 and 8.11, Sasaki *et al.* [275] predict an interesting chiral angle dependence of the TO mode softening. Future experiments on structurally identified and truly isolated individual (n, m) nanotubes, while challenging, will certainly shed light on this topic.

Similar experiments on semiconducting nanotubes reveal that their G-band phonons also experience energy renormalization due to electron–phonon coupling [49, 276]. Since $\hbar\omega_{\mathrm{LO/TO}} < E_{11}^{\mathrm{S}}$ for S-SWNTs, the G-band phonons are unable to create real electron–hole excitations across the semiconducting band gap, and as a result there is no lifetime broadening of the phonon. Nonetheless, virtual electron–hole excitations, which do not conserve energy, do contribute to renormalizing the phonon energy [276]. In the case of semiconducting SWNTs both the TO and LO modes couple to intermediate electron–hole pairs with the TO mode experiencing a greater E_{F}-dependent frequency shift. Interestingly, this effect becomes most significant in larger diameter nanotubes as the band gap energy approaches the phonon energy [276]. Therefore the frequency renormalization in semiconducting nanotubes has the opposite diameter dependence to that of metallic SWNTs, and the effect in S-SWNTs is smaller in magnitude than in M-SWNTs.

8.4.4
Chemical Doping of SWNTs

As discussed in Section 8.2.2, low doping levels suppress the Kohn anomaly, thus causing an upshift in the LO G-band frequency for both *p* and *n* doping in SWNTs (see Figure 8.12). However, for higher doping levels the structural distortions are expected to dominate, so that *p* and *n* doping should then cause an upshift and downshift, respectively, in the measured phonon frequencies of SWNTs (see Figure 8.4c). Such *p* or *n* doping behavior has indeed been observed experimentally for the G-band of MWNTs and SWNTs doped chemically to higher doping levels with different atoms, which behave as donors or acceptors to carbon [34, 277]. The dopant-induced interactions (whether it is an inorganic species such as an alkali-metal donor or a halogen acceptor, or an organic polymer chain or a DNA strand) with the sidewall of a nanotube will perturb the Fermi level of the nanotube through charge-transfer interactions. Since electrons and phonons are strongly coupled to each other, these perturbations will influence the various Raman modes present in carbon nanotubes. For example, the doping with alkali metals like K, Rb, and Cs leads to a softening (or downshift) of 35 cm^{-1} (saturated regime) of the G-band frequencies, and is accompanied by dramatic changes in its lineshape. For SWNT bundles doped with halogens (for example, Br_2), an upshift in the Raman-mode frequencies was observed relative to the corresponding frequencies in the pristine bundles. Details about the Raman characterization of doped SWNTs can be found in [34].

8.5 Summary

In this chapter we addressed the effect of time-dependent perturbations to the G-band spectra of graphene and carbon nanotubes. We showed that, when the adiabatic approximation is not valid, electrons and phonons couple, thus changing both the electron energies (Peierls-like effect) and the phonon energies (Kohn anomaly effect). These effects are strongly dependent on gate voltage and temperature, thus making the G-band work as a probe for nanocarbon doping. The Kohn anomaly is observed in metallic systems, where real electron–hole pair creation can occur by a phonon energy ($\hbar\omega_G$) process, thus strongly influencing the G-band frequency and linewidth of graphene and metallic SWNTs. The effects in metallic SWNTs are stronger than in graphene because of the quantum confinement effect, and this process depends sensitively on diameter and chiral angle. In graphene these effects depend on the number of layers. Semiconducting SWNTs also exhibit a phonon energy renormalization due to electron–phonon coupling, but this renormalization effect is weaker than for the metallic SWNTs because no real anomaly takes place ($E_{gap} > \hbar\omega_G$) for S-SWNTs. Consequently, while the G-band linewidth in graphene and metallic SWNTs is strongly sensitive to whether or not the gate voltage matches the energy of the anomaly, in semiconducting SWNTs the G-band linewidth is basically independent of doping. Finally, putting together the rich behavior of the G-band frequency and linewidth, as discussed in Chapters 7 and 8, we conclude that the Raman G-band provides a highly sensitive probe for studying and characterizing nanocarbons.

Problems

[8-1] Calculate the period of the oscillation for the vibration at $1580\,\mathrm{cm}^{-1}$. Also give the frequency in THz. (Use the fact that $1\,\mathrm{eV} = 8650\,\mathrm{cm}^{-1}$.)

[8-2] Estimate the Raman spectral width in cm^{-1} by using the uncertainty relation when the lifetime of the photoexcited carrier is 500 fs. Repeat the calculation for 50 fs.

[8-3] A typical length of a carbon nanotube is 1 μm. How long does it take for the light to go 1 μm. How many times do carbon atoms oscillate at the G-band frequency during this time?

[8-4] What is the maximum velocity or acceleration of the atomic vibration for a phonon of $1580\,\mathrm{cm}^{-1}$? In this calculation, we should consider the number of phonons to be n.

[8-5] When we use the maximum acceleration in the previous problem, evaluate the force that a π electron feels in this acceleration. Compare this force with the Coulomb force in a carbon atom. You can use $Z = 4$ for the screened

ion core and $r = 0.5\,\text{Å}$ for the radius. Check if the Coulomb potential is sufficiently strong to keep the π electron bound to the carbon atom.

[8-6] (Peierls instability) Consider a linear carbon chain in which the nearest neighbor transfer parameters have alternating values: $t_1, t_2, t_1, t_2, \ldots$. Show that in this case, an energy gap is opened at the zone boundary and the value of the energy gap is proportional to $t_1 - t_2$.

[8-7] In the previous problem, let us consider the electron–phonon parameter α such that $t_i = t_0 - \alpha(x_{i+1} - x_i)$, where x_i denotes the lattice distortion. By an alternative lattice distortion, $x_i = x_0(-1)^i$, the total energy of the electron decreases because of the opening an energy gap at the Fermi energy. On the other hand, because of the lattice distortion, the system loses lattice energy which is proportional to $Kx_0^2/2$ per bond (K is the spring constant). By minimizing the total energy, obtain the optimized x and the energy gap.

[8-8] When the temperature of the nanotubes is either high or very low, how does the phonon softening change as a function of the Fermi energy? Using the Fermi distribution function, and explain your result qualitatively.

[8-9] The G-band phonon becomes soft when the temperature becomes high. Explain the mechanism of phonon softening for high temperature.

[8-10] When the Fermi energy changes, how is the electron–phonon interaction suppressed? Explain and plot qualitatively the phonon frequency as a function of the Fermi energy.

[8-11] Show that, for metallic SWNTs, only the phonon causes an electronic gap opening, independent of the tube chiral angle (this is shown in Figure 8.8 for an armchair SWNT). Here you should show the above result for a zigzag and a chiral SWNT.

[8-12] The RBM (radial breathing mode) frequency can be expected to produce phonon softening by changing the Fermi energy. However, the shift of the RBM frequency is known not to be large ($\sim$ 1–3 cm^{-1}). Consider why the phonon softening of the RBM is small. How about the phonon softening for the D or G′-bands?